Unsupervised Deep Learning-based Reconfigurable Intelligent Surface Aided Broadcasting Communications in Industrial IoTs

Son Dinh-Van, Tiep M. Hoang, *Member, IEEE,* Ramona Trestian, *Member, IEEE* and Huan X. Nguyen, *Senior Member, IEEE*

***Abstract*—This paper presents a general system framework which lays the foundation for Reconfigurable Intelligent Surface (RIS)-enhanced broadcast communications in Industrial Internet of Things (IIoTs). In our system model, we consider multiple sensor clusters co-existing in a smart factory where the direct links between these clusters and a central base station (BS) is blocked completely. In this context, an RIS is utilized to reflect signals broadcast from BS toward cluster heads (CHs) which act as a representative of clusters, where BS only has access to the statistical distribution of the channel state information (CSI). An analytical upper bound of the total ergodic spectral efficiency and an approximation of outage probability are derived. Based on these analytical results, two algorithms are introduced to control the phase shifts at RIS, which are the Riemannian conjugate gradient (RCG) method and the deep neural network (DNN) method. While the RCG algorithm operates based on the conventional iterative method, the DNN technique relies on unsupervised deep learning. Our numerical results show that the both algorithms achieve satisfactory performance based on only statistical CSI. In addition, compared to the RCG scheme, using deep learning reduces the computational latency by more than 10 times with an almost identical total ergodic spectral efficiency achieved. These numerical results reveal that while using conventional RCG method may provide unsatisfactory latency, DNN technique shows much promise for enabling RIS in ultra reliable and low latency communications (URLLC) in the context of IIoTs.**

***Index Terms*—Industry 4.0, Industrial Internet of Things, URLLC, Unsupervised Deep Learning, Reconfigurable Intelligent Surface, Smart Factory.**

I. Introduction

Industrial Internet of Things (IIoTs) has recently emerged as a technology that facilitates a paradigm shift in various manufacturing industries towards Industry 4.0. IIoT, as a framework for machines, computers, smart sensors and people, enabling intelligent industrial operations using advanced data analytics for transformational business outcomes. Besides computing, big data and machine learning, wireless communications are also playing an important role in IIoT operations. For example, an intelligent measuring device or a sensor seamlessly sends real-time information about the status of products/machines to the cloud where machine learning can be deployed to support enormous data-driven applications such as automation, maintenance, job scheduling and control. Compared to wired connections, wireless networks have several advantages that facilitate IIoT use cases. For example, wireless solutions allow connections even in large, remote and hard-to-read areas, leading to cost efficiency. Wireless networks also provide connection flexibility in network topology design. Driven by a variety of industrial applications, nevertheless, future wireless networking infrastructure for IIoTs is required to meet stringent requirements. For example, the International Telecommunication Union Radiocommunication Sector (ITU-R) has considered two major usage scenarios for machine-to-machine (M2M) communications including massive machine-type communications (mMTC) and ultra-reliable and low-latency communications (URLLC) [1]. While the former refers to the robust connections to massive devices in industrial scenarios such as mass control, remote machine diagnostics and over-the-air update, the latter targets to applications such as factory automation, telesurgery, etc [2]. Some URLLC use cases also simultaneously require very high data rate (e.g., immersive virtual reality).

Recently, reconfigurable intelligent surface (RIS) has gained a significant interest as a solution to enable a smart radio environment, where the wireless propagation conditions can be co-engineered with the physical layer signals to provide extra wireless communication capabilities. In particular, an RIS device is a planar surface consisting of discrete elements that can be controlled at either an individual or a group level to interact with electromagnetic waves in a desirable manner. For instance, not only can RIS be controlled to focus incident signals toward a certain location [3], but it also benefits the existing wireless communications by reflecting, refracting, absorbing the signals. As a result, it is anticipated that RIS may pave the way for wireless communications in IIoTs because of the following reasons. Firstly, industrial settings often exhibit unique characteristics affecting the radio-wave environment and transmissions due to their physical features such as floor

Son Dinh-Van is with Warwick Manufacturing Group, the School of Engineering, University of Warwick, Coventry, CV4 7AL, U.K. Email: son.v.dinh@warwick.ac.uk.

Tiep M. Hoang is with the School of Electronics and Computer Science, the University of Southampton, Southampton SO17 1BJ, U.K. Email: tiep.hoang@soton.ac.uk.

Ramona Trestian and Huan X. Nguyen are with the London Digital Twin Research Centre, Middlesex University, The Burroughs, London, NW4 4BT, United Kingdom. Email: {r.trestian@mdx.ac.uk, h.nguyen}@mdx.ac.uk.

Huan X. Nguyen is also with Van Lang University, Ho Chi Minh City, Vietnam. Email: hx.nguyen@vlu.edu.vn

This work was supported by a UK-India Education and Research Initiative (UKIERI) grant, ID DST 2018-19-11. The grant is funded by the UK Department for Business, Energy and Industrial Strategy and Department for Education and delivered by the British Council.

The work of Huan X. Nguyen is also supported by collaborative fund from Van Lang University.

Corresponding author: Huan X. Nguyen.

plans, layouts of metallic machines and work-cells. In this context, RIS can help by manipulating the radio waves in accordance with each setting layout. Secondly, RIS is low-cost and sufficiently compact to be equipped at various locations such as walls, ceilings, parts objects, which are normally unattainable regarding installing additional base stations.

Since the design of phase shifts is critical for RIS-assisted communication systems, it has been of interest in a number of studies [4]–[6]. The research proposed in [4] aimed at maximizing the total signal strength received at the user for a point-to-point communication by jointly designing the active beamforming at the access point and passive reflect beamforming by the phase shifters at RIS. A system model where an RIS was deployed to assist the downlink transmission between a base station and multiple users was considered in [5]. The phase shifts were also designed to maximize the sum rate while a zero forcing beamforming was utilized at the BS. In [6], the author concentrated on optimizing the fairness between received signal-to-interference-plus-noise ratio (SINR) of users. In particular, a projected gradient ascent algorithm was used to solve the optimization problem which determined the phases that maximize the minimum user SINR under optimal linear precoder.

Despite providing useful insights, all of the above studies exhibit two concerns which might restrict its implementation in reality. Firstly, these research works assumed a perfect channel state information (CSI) for all RIS-related channels, which is challenging to obtain especially in the case when RIS is equipped with completely passive elements. As a result, there was then a shift of research focus to the cascaded CSI instead of each individual RIS-related channel. Specifically, to obtain the estimation of cascaded channel, the key idea is to divide the estimation process into various stages. In each stage, only one element of RIS was activated, which allows the cascaded CSI associated to that element to be estimated [7], [8]. However, not only does this mechanism require a huge pilot, but the accuracy of estimated CSI might also be degraded. In addition, in the case when RIS is equipped with a large number of elements, the CSI might change before the channel estimation is completed in all the stages. Secondly, to design the phase shifts at RIS, the aforementioned research in [4]–[6] solved the optimization problems by using iterative methods (e.g., semidefinite program with CVX tool in [4], majorization-minimization in [5] and projected gradient ascent in [6]). These approaches are computationally expensive and slow, therefore, it might not be feasible for some specific applications IIoTs such as URLLC.

In this paper, we consider the feasibility of RIS in assisting broadcast communications in a smart factory where the direct links between a central base station (BS) and sensors are blocked completely. In this scenario, all the sensors form different clusters, each has one sensor acting as a cluster head. Moreover, an RIS is utilized to reflect the signal broadcast from BS toward all the cluster heads. The main contributions of our work may now be summarized as follows. **Firstly**, we propose a general system framework for RIS-assisted broadcast channels in IIoTs. This scenario will find various useful applications in emerging IIoTs such as mass control or over-the-air update. Unlike the majority of existing research which assumed the availability of perfect CSI, in this paper, we consider a realistic model in which only the statistical CSI of the RIS-related channels are available. Based on this, a closed-form derivation for the upper bound of total ergodic spectral efficiency (SE) is formulated. In the case when there is a single cluster and RIS is equipped with a sufficiently large number of phase elements, the closed-form approximation for outage probability is also derived. **Secondly**, based on the performance analysis, we introduce two phase shift control algorithms to maximize the total ergodic SE. One algorithm is adopted based on the well-known Riemannian conjugate gradient (RCG) method, which resembles the conventional iterative technique while the other relies on unsupervised deep learning (DL). Whereas the RCG technique is classic and has been used extensively in solving manifold optimization problems, DL utilizes a totally different approach which is necessarily investigated. An initialization method is also proposed to accelerate the conventional RCG scheme. Regarding unsupervised DL, we propose a simple, but effective network structure to compute the phase shift configuration. We also discuss other important aspects such as data normalization which is useful to address the vanishing gradient problem. **Finally**, numerical results are provided to benchmark these algorithms with various important performance criterias in IIoTs such as ergodic SE, outage probability and complexity. It is shown that utilizing machine learning provides a nearly identical performance in comparison to the conventional methods such as RCG algorithm, while offering a significantly reduced running time spent on computing the phase shifts (e.g., 10 times faster). This unfolds the potential of utilizing machine learning for phase shift control in URLLC, which is one of the most important applications in the context of IIoTs.

Notation: Throughout this paper, we use lowercase and uppercase boldface letters to represent vectors and matrices, respectively. The transpose and conjugate-transpose of $\mathbf{X}$ are denoted by $\mathbf{X}^{\mathrm{T}}$ and $\mathbf{X}^{\mathrm{H}}$. The notation $\mathrm{vec}(.)$ is a vectorization operator. In addition, $\mathbf{I}_M$ stands for an $M \times M$ identity matrix while X_{ij} and $\mathbf{X}[n]$ give the (i,j)-th entry and the n-th row of $\mathbf{X}$. Furthermore, $\mathbf{X} \sim \mathcal{CN}(\mathbf{M}, \mathbf{V})$ denotes that $\mathbf{X}$ is a complex Gaussian matrix with mean matrix $\mathbf{M}$ and covariance matrix $\mathbf{V}$. The operator $\odot$ represents component-wise multiplication while $\mathrm{mean}(.)$ and $\mathrm{cov}(.)$ stand for the mean and covariance. Finally, $\mathbb{E}\{.\}$ and $\mathbb{V}\{.\}$ represent the expectation and variance operator, $\|.\|$ is the Euclidean norm while $\Re(.)$ and $\Im(.)$ denote the real and imaginary operator.

II. System Model

In this paper, we consider a downlink broadcast wireless communication system in IIoTs, which comprises K sensor clusters and one central BS. Each cluster consists of a certain number of sensors with one of them acting as a representative node, so-called cluster head (CH). The CHs are responsible for communicating with BS on behalf of other sensors within its cluster. In this setup, BS broadcasts signals to K CHs in the same time-frequency resource. In the context of IIoTs, each sensor takes turn to be CH of its cluster. This system

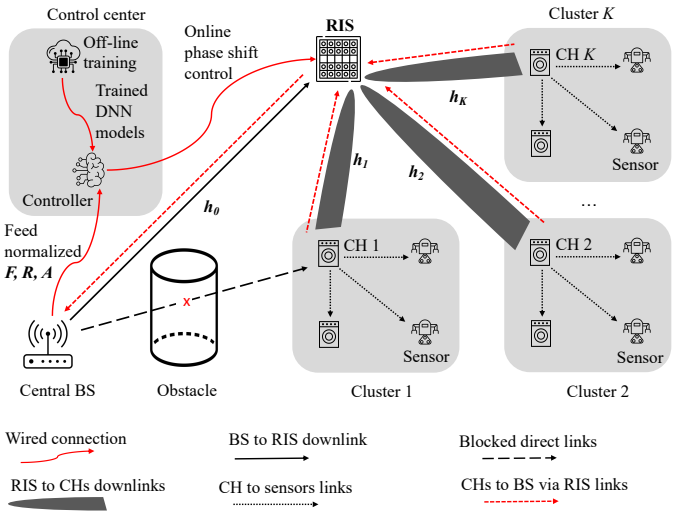

Fig. 1. The system model of RIS-assisted broadcast communications in smart factory with machine learning.

model reflects various useful use cases (e.g., BS needs to frequently send the control/safety signals to all CHs; an over-the-air update needs to be performed on the entire factory; or BS broadcasts multimedia contents, etc). In addition, we also consider a scenario which is normally encountered in industrial plants, in which the line of sight (LOS) links between the sensors and BS are blocked completely due to obstacles (Fig. 1). As a consequence, an RIS is installed at a desirable position (e.g., ceilings, walls, etc) in the area to passively support the connection between BS and K CHs. Each sensor and BS are equipped with a single antenna whereas RIS avails of a uniform linear array (ULA) of M reflecting elements whose phases can be controlled by an external software (namely Controller). Controller is connected with BS and RIS via wired connection. In this work, we consider that all the phase elements equipped at RIS are completely passive.

Hereafter, CHs and clusters are denoted by their indexes (e.g., CH k and cluster k are the k-th CH and the k-th cluster.)

A. Channel Model

For the sake of tractability, we use subscript 0 to represent the terms related to the link between RIS and BS, while subscript k to describe the link between RIS and CH k with $1 \leq k \leq K$. In this work, the complex channel vector between RIS and CH k is modeled as

$$\mathbf{h}_k = \sqrt{\beta_k}\left(\sqrt{\frac{\mathcal{K}_k}{\mathcal{K}_k+1}}\,\mathbf{a}_k + \sqrt{\frac{1}{\mathcal{K}_k+1}}\,\mathbf{z}_k\right), \quad (1)$$

where $1 \leq k \leq K$ and $\mathcal{K}_k$ stands for the Rician $\mathcal{K}$-factor whereas β_k denotes the large scale fading coefficient of the link between CH k and RIS. In addition, $\mathbf{a}_k$ and $\mathbf{z}_k$ correspond to the LOS and non-LOS (NLOS) components, respectively. It is assumed that $\mathbf{z}_k \sim \mathcal{CN}(\mathbf{0}_M, \mathbf{I}_M)$.

Similarly, the channel vector between RIS and BS is modeled as follows

$$\mathbf{h}_0 = \sqrt{\beta_0}\left(\sqrt{\frac{\mathcal{K}_0}{\mathcal{K}_0+1}}\,\mathbf{a}_0 + \sqrt{\frac{1}{\mathcal{K}_0+1}}\,\mathbf{z}_0\right), \quad (2)$$

The deterministic vector $\mathbf{a}_k$ whose components are given by the response of ULA, which is presented by [9]

$$\begin{aligned}\mathbf{a}_k &= \mathbf{a}(\sin(\omega_k), M) \\ &= \left[1,\ e^{-j\frac{2\pi d}{\lambda}\sin(\omega_k)},\ \cdots, e^{-j(M-1)\frac{2\pi d}{\lambda}\sin(\omega_k)}\right]^{\mathrm{T}}, \quad (3)\end{aligned}$$

where ω_0 is the angle of arrival (AoA) of the signal radiated from BS to RIS and ω_k $(k>0)$ is the AoD of signal reflected from RIS to CH k while d is the antenna separation and λ is the carrier wavelength. Moreover, we consider low mobility scenarios, which means that $\mathbf{a}_k, \mathcal{K}_k$ and β_k change very slowly with respect to time and can be assumed to be deterministic for the signal processing duration of interest. This means that it is feasible to obtain the statistical CSI since its distribution varies slowly, hence no frequent update is required, which substantially reduces the training overhead.

Let us denote $\bar{\mathbf{h}}_k \triangleq \sqrt{\frac{\beta_k\mathcal{K}_k}{\mathcal{K}_k+1}}\,\mathbf{a}_k$ and $\widetilde{\mathbf{h}}_k \triangleq \sqrt{\frac{\beta_k}{\mathcal{K}_k+1}}\,\mathbf{z}_k$. As a result, $\mathbf{h}_k$ can be rewritten as $\mathbf{h}_k = \bar{\mathbf{h}}_k + \widetilde{\mathbf{h}}_k$. Obviously, $\bar{\mathbf{h}}_k$ is a deterministic vector and $\widetilde{\mathbf{h}}_k \sim \mathcal{CN}(\mathbf{0}_M, \mathbf{\Sigma}_k)$ with $\mathbf{\Sigma}_k \triangleq \frac{\beta_k}{\mathcal{K}_k+1}\,\mathbf{I}_M$.

Since the direct paths between BS and CHs are blocked completely due to obstacles, the signal received at CH k is reflected by RIS, which can be expressed as

$$y_k \triangleq \left(\mathbf{h}_k^{\mathrm{H}}\mathbf{\Phi}\mathbf{h}_0\right)x + n_k, \quad (4)$$

where $\mathbf{\Phi} = \mathrm{diag}\,(\boldsymbol{\phi})$ with $\boldsymbol{\phi} \triangleq \left[e^{j\phi_1}, e^{j\phi_2}, ..., e^{j\phi_M}\right]^{\mathrm{T}}$ and $\phi_i \in [0, 2\pi]$. The matrix $\mathbf{\Phi}$ captures the phase shifts applied by all reflecting elements of RIS. In addition, x is the broadcast signal transmitted by BS, such as $x = \sqrt{\mathrm{P}}s$, where s is the data symbol satisfying $\mathbb{E}\{\|s\|^2\} = 1$ and P is the transmit power of BS while n_k is the additive noise at CH k, $n_k \sim \mathcal{CN}(0, \sigma^2)$ with σ^2 being the noise power.

The instantaneous signal-to-noise ratio (SNR) of the transmission for CH k can be written as

$$\gamma_k(\mathbf{\Phi}) \triangleq \frac{\mathrm{P}}{\sigma^2}\left\|\mathbf{h}_k^{\mathrm{H}}\mathbf{\Phi}\mathbf{h}_0\right\|^2. \quad (5)$$

B. Transmission Protocol

We assume that all the BS, CHs and sensors are perfectly synchronized[1] and operate with a TDD protocol. In addition, frame-based transmission is considered in which the length of each frame is fixed. Despite of focusing on the broadcast downlink transmission in this paper, we provide a detailed description for the entire transmission protocol, which consists of three phases. More precisely:

- First phase - *uplink transmission:* In this phase, one sensor is assigned to be a CH for each cluster. These K CHs are responsible for communicating with BS on behalf of other sensors in its cluster. By doing this, the energy consumption of sensors is minimized by having them only communicate with its CH. Nevertheless, CHs still consume a relatively greater amount of energy than the other sensors since they have to communicate with

[1]There were several synchronization protocols proposed in the context of the cluster-based IoT networks such as E-SATS [10], CMTS [11] and CCTS [12].

BS which is further away. As a result, in order to prolong the network lifetime, each sensor takes turns to undertake the role of CH to balance the energy consumption level among themselves in each time frame [13]. Following by this CH assignment procedure, all the CHs will transmit the collected data and notify their roles to BS while other sensors are staying idle for the sake of energy conservation. Since the direct links between BS and all the CHs are blocked completely, these transmissions are performed with the aid of RIS. Based on the signals received from the K CHs, BS estimates the distribution for all the channels associated to each CH. This is possible because of the two following reasons. Firstly, compared to the small-scale CSI, large-scale coefficients vary much more slowly during a significantly longer period. Secondly, it was shown in [14] that the RIS can be fabricated so that the channels are reciprocal in commonly designed RIS-assisted communication networks.

- Second phase - *broadcast downlink transmission:* In this paper, we focus on this phase in which the broadcast downlink transmission is performed under the cooperation of BS, RIS and Controller. In particular, for each time slot, BS sends important coefficients computed from the estimated channel distribution to Controller via wired connection. Next, Controller is responsible for computing the RIS configuration so that the broadcasted signal is reflected effectively toward CHs. We note that during this phase, except for CHs which are active to receive signals from BS, other sensors stay idle to save the energy consumption. It is also worth noting that the configuration of RIS is not kept fixed forever but it is updated at a low rate and requires a lower estimation and feed back overhead compared to estimating instantaneous CSI. This significantly relaxes the need of frequently reconfiguring the RIS, which is one of the most critical issues in RIS-assisted wireless communication systems.
- Third phase - *multihop broadcast transmission:* The broadcast signals are disseminated over the entire network in this phase. In particular, each CH is responsible for sending the broadcast signal to all the sensors within its cluster. At this stage, multihop broadcasting might also be performed by sensors which received the signal successfully. Since this phase has been studied extensively in literature [15], [16], we do not focus on this phase in the scope of this paper.

III. Performance Analysis and Problem Formulation

In this section, we derive closed-form expressions for the expectation of signal strength, the upper bound of the total ergodic spectral efficiency (SE) and outage probability which enable us to obtain important insights as well as the design of phase shifts within our system.

A. SNR Analysis

Lemma 1. *For any given arbitrary settings of phase shift elements at RIS, the expectation of SNR for the transmission to CH k is expressed as*

$$\mathbb{E}\{\gamma_k(\boldsymbol{\phi})\} = f_k + r_k \times \left\|\widetilde{\mathbf{a}}_k^{\mathrm{H}}\boldsymbol{\phi}\right\|^2, \tag{6}$$

where

$$f_k \triangleq \frac{\mathrm{P}}{\sigma^2} M\beta_0\beta_k \frac{\mathcal{K}_0+\mathcal{K}_k+1}{(\mathcal{K}_0+1)(\mathcal{K}_k+1)}, \tag{7}$$

$$r_k \triangleq \frac{\mathrm{P}}{\sigma^2} \beta_0\beta_k \frac{\mathcal{K}_0\mathcal{K}_k}{(\mathcal{K}_0+1)(\mathcal{K}_k+1)}, \tag{8}$$

and the cascaded angle

$$\widetilde{\mathbf{a}}_k \triangleq \mathbf{a}_k^{\mathrm{H}} \odot \mathbf{a}_0, \quad \widetilde{\mathbf{a}}_k \in \mathbb{C}^{M\times 1}. \tag{9}$$

Proof. See Section VIII-A. □

B. Ergodic SE Analysis

For a given phase shift configuration, the ergodic SE of the transmission for CH k is expressed as

$$\begin{aligned} R_k(\boldsymbol{\Phi}) &\triangleq \mathbb{E}\left\{\log_2(1+\gamma_k)\right\} \\ &= \mathbb{E}\left\{\log_2\left(1+\frac{\mathrm{P}}{\sigma^2}\left\|\mathbf{h}_k^{\mathrm{H}}\boldsymbol{\Phi}\mathbf{h}_0\right\|^2\right)\right\}. \end{aligned} \tag{10}$$

As a result, the total ergodic SE of the entire broadcast system can be described by

$$R(\boldsymbol{\Phi}) \triangleq \sum_{k=0}^{K} \mathbb{E}\left\{\log_2\left(1+\frac{\mathrm{P}}{\sigma^2}\left\|\mathbf{h}_k^{\mathrm{H}}\boldsymbol{\Phi}\mathbf{h}_0\right\|^2\right)\right\}. \tag{11}$$

Due to the presence of logarithmic expression, it is challenging to derive the close-form formula for (11). To overcome this issue, we aim at finding a tight and tractable upper bound for the total ergodic SE.

Lemma 2. *For any given arbitrary settings of phase shift elements at RIS, the total ergodic SE of the broadcast system is upper bounded by*

$$\bar{R}(\boldsymbol{\phi}) \triangleq \sum_{k=1}^{K} \log_2\left(1+f_k+r_k\left\|\widetilde{\mathbf{a}}_k^{\mathrm{H}}\boldsymbol{\phi}\right\|^2\right). \tag{12}$$

Proof. See section VIII-B. □

C. Outage Probability Analysis

The outage probability of the broadcast transmission from BS to CH k can be defined as the probability that its achievable SE is lower than a predefined threshold $R_{\mathrm{th},k}$, which is expressed as

$$\begin{aligned} \mathrm{P}_{\mathrm{out},k} &\triangleq \Pr\left\{\log_2\left(1+\gamma_k\right) < R_{\mathrm{th},k}\right\} \\ &= \Pr\left\{\left\|\mathrm{X}_k\right\|^2 < \frac{\sigma^2}{\mathrm{P}}\left(2^{R_{\mathrm{th},k}}-1\right)\right\}, \end{aligned} \tag{13}$$

where X_k is a complex random variable (RV) representing the combined channel coefficient, i.e., $\mathrm{X}_k = \mathbf{h}_k^{\mathrm{H}}\boldsymbol{\Phi}\mathbf{h}_0$.

Unfortunately, obtaining a closed-form solution for the cummulative distribution function (CDF) of X_k in elementary functions appear to be infeasible due to X_k contains the sum of the product of non-identical Rician distributions. However, in the case when the number of phases at RIS is sufficiently large,

its closed-form expression can be approximated by using the moment matching approximation and central limit theorem.

Lemma 3. *Given a sufficiently large RIS, the outage probability of the transmission for CH k is approximated as*

$$\mathrm{P}_{\mathrm{out},k}(\boldsymbol{\phi}) \approx 1 - Q_1\left(\sqrt{2\frac{r_k}{f_k}}\left\|\widetilde{\mathbf{a}}_k^{\mathrm{H}}\boldsymbol{\phi}\right\|, \sqrt{\frac{2^{R_{\mathrm{th},k}+1}-2}{f_k}}\right), \quad (14)$$

where $Q(.)$ denotes the Marcum-Q function defined as

$$Q_M(a,b) = 1 - e^{-a^2/2}\sum_{k=0}^{\infty}\left(\frac{a^2}{2}\right)^k \frac{\gamma(M+k, b^2/2)}{k!}, \quad (15)$$

with $\gamma(s,x)$ being the regularized Gamma function.

Proof. See Section VIII-C. □

In the broadcast system, since the nodes are capable of performing multihop broadcast transmission, it is more meaningful to investigate the outage probability of the entire broadcasting phase. In particular, the outage probability of this phase can be defined as the probability that the average achievable SE of all links is lower than a pre-defined threshold R_{th}, which can be written as

$$\mathrm{P}_{\mathrm{out}} \triangleq \Pr\left\{\frac{1}{K}\sum_{k=0}^{K}\log_2(1+\gamma_k) < R_{\mathrm{th}}\right\}. \quad (16)$$

It is challenging to acquire a closed-form solution for (16) due to the sum of logarithmic terms which contain non-identical Chi-square distributions. However, in the special case when $K = 1$, the equation (16) reduces to (13), which was adressed in Lemma 3. In the case when $K > 1$, numerical results can be computed via simulations.

D. Discussions

Based on the analysis of SNR, the upper bound of the total ergodic spectral effciency and outage probability, we highlight some important insights as follows

Remark 1. *Regardless of any settings for the phase shifts at RIS, the term f_k scales proportionally with the number of elements M at RIS. However, f_k contains the product of path-loss coefficients β_0 and β_k, which are extremely small. This indicates that in the case when M is not suficiently large, the term f_k is very low. By contrast, when $M \to \infty$, it is obvious that $\mathbb{E}\{\gamma_k(\boldsymbol{\phi})\} \to \infty$, $\bar{R}(\boldsymbol{\phi}) \to \infty$ and $\mathrm{P}_{\mathrm{out},k} \to 0$.*

Proposition 1. *In the case when there is only one CH, the optimal performance (i.e., the upper bound of the total ergodic capacity, the expectation of SNR and the outage probability) is acquired when the term $\left\|\widetilde{\mathbf{a}}_k^{\mathrm{H}}\boldsymbol{\phi}\right\|$ is maximized. It is not difficult to show that in this case, the optimal phase shifts are $\boldsymbol{\phi}_{\mathrm{opt},K=1} \triangleq \angle\widetilde{\mathbf{a}}_k$ and the corresponding optimal performance can be calculated as*

$$\mathbb{E}\{\gamma_k(\boldsymbol{\phi}_{\mathrm{opt},K=1})\} = f_k + r_k\left\|\widetilde{\mathbf{a}}_k\right\|^2, \quad (17)$$

$$\bar{R}(\boldsymbol{\phi}_{\mathrm{opt},K=1}) = \log_2\left(f_k + r_k\left\|\widetilde{\mathbf{a}}_k\right\|^2\right), \quad (18)$$

$$\mathrm{P}_{\mathrm{out},k}(\boldsymbol{\phi}_{\mathrm{opt},K=1}) = 1 - Q_1\left(\sqrt{2\frac{r_k}{f_k}}\left\|\widetilde{\mathbf{a}}_k\right\|, \sqrt{\frac{2^{R_{\mathrm{th},k}+1}-2}{f_k}}\right) \quad (19)$$

This points out that if the phases of RIS are controlled optimally, the expectation of received SNR and the ergodic SE increase linearly with M and $\log_2 M$, respectively.

E. Problem Formulation

The sum-rate maximization and its similar forms have many applications in wireless communications systems. It allows us to obtain the optimal design for various aspects in a network system, such as power control [17], [18], resource management [19], etc. In the context of broadcast system in IIoTs, by maximizing the total SE, we guarantee that the number of CHs receiving broadcast signals successfully is as many as possible. Then these CHs in turn broadcast the received signal to other sensors, as described in the multihop broadcast transmissions phase. It is also worth mentioning that a high SE is required in many applications in IIoTs such as over-the-air update, multimedia streaming and safety control. In addition, unlike the outage probability which normally contains intractable mathematical derivation, the SE allows us to obtain further analysis and efficient design of the RIS configurations.

Proposition 1 indicates the importance of phase shift control in the considered system model. Therefore, in this paper, without the perfect CSI knowledge, we aim at controlling the phase shifts at RIS to maximize the total ergodic SE. This is equivalent to

$$(\mathrm{P0}) \quad \max_{\boldsymbol{\Phi}} \quad R(\boldsymbol{\Phi}) \quad (20a)$$

$$\text{s.t} \quad |\Phi_{ii}|^2 = 1, \quad \forall i \quad (20b)$$

$$|\Phi_{ij}| = 0, \quad \forall i \neq j. \quad (20c)$$

In general, solving this optimization is challenging since the objective function (20a) contains the expectation term which is difficult to obtain its closed-form expression. Therefore, we focus on solving an suboptimal optimization problem in which the upper bound of the total ergodic SE is maximized. Later, we will show that this technique also improves the performance significantly via simulations. The new optimization problem now can be formulated as

$$(\mathrm{P1}) \quad \max_{\boldsymbol{\phi}} \quad \sum_{k=1}^{K}\log_2\left(1 + f_k + r_k\left\|\widetilde{\mathbf{a}}_k^{\mathrm{H}}\boldsymbol{\phi}\right\|^2\right) \quad (21a)$$

$$\text{s.t} \quad |\phi_i|^2 = 1, \quad \forall i. \quad (21b)$$

It is worth noting that the optimization problem (P1) is non-convex due to the presence of phase shifts. In particular, the main obstacles are the unit modulus constraints (21b), which form a complex circle manifold. Despite this challenge, we investigate two algorithms for potential solutions: one is Riemannian conjugate gradient (RCG) method which was frequently adopted in literature and the other is based on the DL technique. The RCG method operates relied on an iterative update of the phase shifts, which might lead to high-latency for phase shift control in many cases. In comparison, the DL method aims at learning the general pattern between the channel coefficients and the optimal phase shifts. It is anticipated that the DL technique might be significantly faster since it only needs one inference to compute the optimal

phases. Therefore, it is natural that these two approaches are totally different and worth being investigated.

IV. Phase Shift Control Using Riemannian Conjugate Gradient

In this section, the conventional iterative method used for phase shift control is adopted. In this type of algorithm, a near-optimal solution can be found by updating variables iteratively until the objective function converges. We propose a manifold optimization algorithm to solve (P1) based on the RCG technique. More background on RCG method can be found in [20]–[22] and there are also some recent applications in wireless communications systems [23], [24].

We start by rewriting the optimization problem (P1) as

$$\text{(P2)} \quad \min_{\boldsymbol{x}} \quad f(\boldsymbol{x}) \tag{22a}$$

$$\text{s.t} \quad \boldsymbol{x} \in \mathcal{M} \tag{22b}$$

where $\boldsymbol{x} \triangleq \boldsymbol{\phi}$, $f(\boldsymbol{x}) \triangleq -\sum_{k=1}^{K} \log_2\left(1 + f_k + r_k \left\|\widetilde{\mathbf{a}}_k^{\mathrm{H}} \boldsymbol{x}\right\|^2\right)$ and $\mathcal{M} \triangleq \{\boldsymbol{x} \in \mathbb{C}^{M\times 1} : |x_i|^2 = 1, \quad \forall i\}$. We say that $\mathcal{M}$ defines a Riemannian manifold and $\boldsymbol{x}$ is a point on $\mathcal{M}$. In addition, for any point $\boldsymbol{x}_k$ on $\mathcal{M}$, its tangent space is denoted as $\mathcal{T}_{\boldsymbol{x}_k}\mathcal{M}$. In particular, $\mathcal{T}_{\boldsymbol{x}_k}\mathcal{M}$ is an Euclidean space defined as a set of all the tangent vectors passing through $\boldsymbol{x}_k$ tangentially with respect to $\mathcal{M}$. Each tangent vector represents one direction along which one can move from $\boldsymbol{x}_k$ to optimize the objective function $f(\boldsymbol{x})$. The Riemannian gradient of f at $\boldsymbol{x}_k$, denoted by $\mathrm{grad}_{\boldsymbol{x}_k} f$, is the orthogonal projection of the Euclidean gradient $\triangledown_{\boldsymbol{x}_k} f$ onto the tangent space $\mathcal{T}_{\boldsymbol{x}_k}\mathcal{M}$. In other words, the Riemannian gradient at a point $\boldsymbol{x}_k$ on the manifold $\mathcal{M}$ is given by

$$\mathrm{grad}_{\boldsymbol{x}_k} f = \triangledown_{\boldsymbol{x}_k} f - \Re\{\triangledown_{\boldsymbol{x}_k} f \odot \boldsymbol{x}_k^*\} \odot \boldsymbol{x}_k, \tag{23}$$

where the Euclidean gradient of the objective function in (P2) at the point $\boldsymbol{x}_k$ can be calculated as

$$\triangledown_{\boldsymbol{x}_k} f = -2\log_2(e) \sum_{k=0}^{K} \frac{r_k \widetilde{\mathbf{a}}_k \widetilde{\mathbf{a}}_k^{\mathrm{H}} \boldsymbol{x}_k}{1 + f_k + r_k \left\|\widetilde{\mathbf{a}}_k^{\mathrm{H}} \boldsymbol{x}_k\right\|^2}. \tag{24}$$

Let $\boldsymbol{d}_k$ be the search direction at the point $\boldsymbol{x}_k$. Note that $\boldsymbol{d}_k$ and $\boldsymbol{d}_{k+1}$ lie in two different tangent spaces $\mathcal{T}_{\boldsymbol{x}_k}\mathcal{M}$ and $\mathcal{T}_{\boldsymbol{x}_{k+1}}\mathcal{M}$, which means that the elementary operations can not be performed directly. To handle this, a mapping technique from a tangent space to another tangent space is utilized [20], so-called *vector transport*. In particular, for a manifold $\mathcal{M}$, the vector transport for a search direction at $\boldsymbol{x}_k$ is given by

$$\mathcal{T}_{\boldsymbol{x}_k \to \boldsymbol{x}_{k+1}}(\boldsymbol{d}_k) \triangleq \mathcal{T}_{\boldsymbol{x}_k}\mathcal{M} \to \mathcal{T}_{\boldsymbol{x}_{k+1}}\mathcal{M} : \tag{25}$$
$$\boldsymbol{d}_k \to \boldsymbol{d}_k - \Re\{\boldsymbol{d}_k \odot \boldsymbol{x}_{k+1}^*\} \odot \boldsymbol{x}_{k+1}.$$

Now, the update rule for the search direction on manifolds is written as

$$\boldsymbol{d}_{k+1} = -\mathrm{grad}_{\boldsymbol{x}_{k+1}} f + \beta_k \mathcal{T}_{\boldsymbol{x}_k \to \boldsymbol{x}_{k+1}}, \tag{26}$$

where β_k can be selected to avoid the ill-conditioned phenomenon and achieve faster convergence. In particular, β_k can be computed using either Polak–Ribière or Fletcher-Reeves formula [25]. Nevertheless, we choose the Polak–Ribière method because it yields more robust and faster convergence [25], where β_k is obtained as

$$\beta_k = \frac{\mathrm{grad}_{\boldsymbol{x}_{k+1}}^{\mathrm{T}} f \left(\mathrm{grad}_{\boldsymbol{x}_{k+1}} f - \mathrm{grad}_{\boldsymbol{x}_k} f\right)}{\mathrm{grad}_{\boldsymbol{x}_k}^{\mathrm{T}} f \cdot \mathrm{grad}_{\boldsymbol{x}_k} f}. \tag{27}$$

Once the search direction $\boldsymbol{d}_k$ at $\boldsymbol{x}_k$ is obtained, *retraction* is utilized to determine the destination on the manifold when moving along a tangent vector. In other words, retraction maps a vector from the tangent space onto the manifold. Particularly, the retraction of a tangent vector $\alpha_k \boldsymbol{d}_k$ at point $\boldsymbol{x}_k$ can be written as

$$\mathcal{R}_{\boldsymbol{x}_k} \triangleq \mathcal{T}_{\boldsymbol{x}_k}\mathcal{M} \to \mathcal{M} : \tag{28}$$
$$\alpha_k \boldsymbol{d}_k \to \mathcal{R}_{\boldsymbol{x}_k}(\alpha_k \boldsymbol{d}_k) = \mathrm{vec}\left[\frac{(\boldsymbol{x}_k + \alpha_k \boldsymbol{d}_k)_i}{|(\boldsymbol{x}_k + \alpha_k \boldsymbol{d}_k)_i|}\right].$$

Here, $\alpha_k > 0$ is a step size that can be searched such that the slope of f in the direction $\boldsymbol{d}_k$ is as low as possible. This can be obtained by using the Armijo rule, i.e., α_k can be determined as the largest number $\alpha_k \in \{1, \beta, \beta^2, \cdots\}$ such that the following inequality holds

$$f(\boldsymbol{x}_k + \alpha_k \boldsymbol{d}_k) - f(\boldsymbol{x}_k) \leq c_1 \alpha_k \ \mathrm{grad}_{\boldsymbol{x}_k}^{\mathrm{T}} f \cdot \boldsymbol{d}_k, \tag{29}$$

with β, c_1 are the pre-defined constant in $[0, 1]$.

Based on these key steps used in each iteration of the manifold optimization, the algorithm used for solving (P2) is summarized in Algorithm 1.

Algorithm 1: RCG algorithm based on Riemannian conjugate gradient method.

Initialization: $\boldsymbol{x}_0 \in \mathcal{M}$; $\beta, c_1 \in [0, 1]$; a maximum number of iterations N_{iter} and a tolerance ε;
Set $k = 0$ and compute $\boldsymbol{d}_0 = -\mathrm{grad}_{\boldsymbol{x}_k} f$;
repeat
  Search a largest step size $\alpha_k \in \{1, \beta, \beta^2, \cdots\}$ satisfying Armijo rule specified in (29);
  Compute the next point $\boldsymbol{x}_{k+1}$ using retraction in (28): $\boldsymbol{x}_{k+1} = \mathcal{R}_{\boldsymbol{x}_k}(\alpha_k \boldsymbol{d}_k)$;
  Compute Riemannian gradient $\mathrm{grad}_{\boldsymbol{x}_{k+1}} f$ by (23);
  Compute vector transport $\mathcal{T}_{\boldsymbol{x}_k \to \boldsymbol{x}_{k+1}}(\boldsymbol{d}_k)$ by (25);
  Compute Polak–Ribière parameter β_k using (27);
  Compute conjugate search direction by using (26);
  Set $k \leftarrow k + 1$;
until $\left\|\mathrm{grad}_{\boldsymbol{x}_k} f\right\| \leq \varepsilon$ or $k > N_{\mathrm{iter}}$;
Take $\boldsymbol{x}_{k+1}$ as the main diagonal elements of matrix $\boldsymbol{\Phi}$.

Discussions: Algorithm 1 requires an initialization for the phase shifts at RIS. Obviously, the convergence will be faster if the variable is initialized so that it is as close to the optimal solution as possible. Therefore, instead of utilizing random phase shifts as an initialized value, we use Proposition 1 to obtain a customized initialization. Suppose that RIS can be divided into K sub-RIS arrays (each serving one CH) and each array has an identical number of elements. Proposition 1 can then be used to obtain the phase shift configuration for each sub-RIS. This phase shift setting is closer to the optimal solution than a random initialization. As a result,

this configuration can be used as an effective initialization to accelerate Algorithm 1. It is formulated as

$$\boldsymbol{x}_0 = \mathrm{vec}\left(\left[\angle\widetilde{a}_{k0},\ \angle\widetilde{a}_{k1}, \cdots,\ \angle\widetilde{a}_{k\lfloor\frac{M}{K}\rfloor}\right]^{\mathrm{T}}\right), \tag{30}$$

where $\lfloor\cdot\rfloor$ denotes the floor function.

It is worth noting that in the case when $K = 1$, optimal performance can be achieved due to the proposed initialization technique. Obviously, the proposed RCG algorithm requires updating the variable $\boldsymbol{x}_k$ iteratively. Importantly, based on extensive experiments, we also observe that there are cases when there does not exist any step sizes satisfying the Armijo condition, causing a poor convergence or numerous iterations required to converge to a local optima. This is a significant weakness of Algorithm 1, which might lead to a high-latency in practice. To overcome this limitation, we will investigate the use of machine learning in the next section.

V. Phase Shift Control with Unsupervised Deep Learning

In this section, we present an overview of the unsupervised DL technique. Subsequently, a detailed description of our proposed unsupervised deep neural network (DNN) used to determine the phase shifts for the RIS by solving the optimization (P1) will be introduced. In addition, the detailed mechanism for data processing, training as well as online inference are also discussed.

A. Unsupervised DL For Solving Optimization Problem

Let ρ be a tensor containing all parameters of the optimization problem in a certain state and $\mathcal{P}$ represents the set of tensors containing parameters collected from various scenarios. In the context of unsupervised DL, $\mathcal{P}$ can be refered to the training data set. In addition, we assume that x_{opt} is the optimal solution when the input parameter is ρ and $\mathcal{X}$ denotes the set of optimal solutions corresponding to $\mathcal{P}$. For each ρ, unsupervised DL aims at generating x_{opt} so that the objective function is minimized without any lables. To this end, the loss function used for the DNN can be set to the objective function, which is denoted as $\mathcal{L}(\rho, x_{\mathrm{opt}})$. In each epoch, the DNN iteratively learns the mapping from $\mathcal{X}$ to $\mathcal{P}$, so-called $\mathrm{f}_{\mathrm{NN}}(.)$, by minimizing the mean of the loss values, e.g., $\mathcal{L}(\mathcal{P};\mathcal{X}) = \frac{1}{|\mathcal{P}|}\sum_{\rho\in\mathcal{P}}\mathcal{L}(\rho; x_{\mathrm{opt}})$. Regrading (P1), ρ can be constructed from the coefficients estimated in each time slot, e.g., $\rho = \{\beta_k, \mathcal{K}_k, \mathbf{a}_k\}$ while x_{opt} is the optimal phase shifts $\{\boldsymbol{\phi}_{\mathrm{opt}}\}$ which will be configured for the broadcast transmission in that timeslot.

B. Proposed Unsupervised DNN Structure

The first intuition perceived from computing the desired phase shifts is that the inputs of DNN should contain all coefficients to learn the mapping $\mathrm{f}_{\mathrm{NN}}(.)$, e.g., $\rho = \{\beta_k, \mathcal{K}_k, \mathbf{a}_k\}$. With this design, the inputs might contain abundant information to determine the phase shifts. Nevertheless, there are various ways to construct the inputs of DNN based on ρ and this is also one of the most important steps to build $\mathrm{f}_{\mathrm{NN}}(.)$. For example, a common method to construct the inputs is to vectorize all of the coefficients available in ρ [26]. Unfortunately, this input design does not show any structures or meaningful patterns in solving (P1). Via empirical experiments, we notice that the DNN had barely learned from this inputs since it was unable to escape from the local optima even when a huge training data was used and after extensive paremeters tuning process. By constrast, instead of utilizing all the important coefficients to construct the inputs, based on the observation of (P1), the efficient input structure of the inputs can be designed based on the parameters $f_k, r_k, \widetilde{\mathbf{a}}_k$. In other words, the effective inputs of DNN can be represented as

$$\rho_{\mathrm{input}} \triangleq \{\mathbf{F}, \mathbf{R}, \mathbf{A}\}, \tag{31}$$

where

$$\begin{aligned}
&\mathbf{F} \triangleq [f_1, f_2, \cdots, f_K]^{\mathrm{T}} \in \mathbb{R}^{K\times 1},\\
&\mathbf{R} \triangleq [r_1, r_2, \cdots, r_K]^{\mathrm{T}} \in \mathbb{R}^{K\times 1},\\
&\mathbf{A} \triangleq [\widetilde{\mathbf{a}}_1, \widetilde{\mathbf{a}}_2, \cdots, \widetilde{\mathbf{a}}_K]^{\mathrm{H}} \in \mathbb{C}^{K\times M}.
\end{aligned} \tag{32}$$

One benefit of this design is that it only requires the knowledge of the cascaded angle $\widetilde{\mathbf{a}}_k$ instead of each individual angle $\mathbf{a}_k$. This facilitates the general design of our system since obtaining the estimation of cascaded angle is more feasible than achieving the knowledge of each individual angle. Let b stand for the batch size, the proposed inputs are 3 three-dimensional tensors whose shapes are $(b, K, 1), (b, K, 1)$ and (b, K, M).

Once $\mathbf{A}$ is fed into the DNN, $\mathbf{A}$ will be extracted into 2 tensors, namely $\mathbf{A}_{\mathrm{re}}$ and $\mathbf{A}_{\mathrm{imag}}$ which are the real and imaginery parts of tensor $\mathbf{A}$, respectively. Subsequently, all of the tensors $\mathbf{A}_{\mathrm{re}}, \mathbf{A}_{\mathrm{imag}}, \mathbf{F}$ and $\mathbf{R}$ will be flattened and concatenated, which constructs the first layer of a fully connected multilayer perceptron (MLP). In particular, the first layer of this MLP consists of $2K(M+1)$ nodes and there are L hidden layers in the MLP. We denote the number of nodes in the k-th layer as l_k. If the k-th layer is a hidden layer, its output is calculated as follows:

$$\mathbf{c}_k = \mathrm{ReLU}\left(\mathrm{BN}\left(\mathbf{W}_k\mathbf{c}_{k-1} + \mathbf{b}_k\right)\right), \tag{33}$$

where $\mathbf{c}_k$ is the output vectors at the k-th layer with the dimension of $l_k \times 1$; $\mathbf{W}_k$ is the $l_k \times k_{k-1}$ weight matrix and $\mathbf{b}_k$ is the $l_k \times 1$ bias vector; $\mathrm{BN}(.)$ denotes batch normalization while $\mathrm{ReLU}(.)$ is the Rectified Linear Unit function which introduces nonlinearity to the network. Let $L-1$ be the number of hidden layers in the MLP. Our fine-tuning process indicated that a satisfactory DNN can still be acquired with a low value of L.

Since the phase shifts $\{\phi_i\}$ are complex numbers satisfying $|\phi_i|^2 = 1$, it cannot be generated directly by a DNN. However, each ϕ_i can still be specified by its normalized phase, i.e., $\phi_i = \exp(2\pi j\hat{\phi}_i)$ with $\hat{\phi}_i \in [0, 1]$. Therefore, we let $\hat{\boldsymbol{\phi}} \triangleq \left[\hat{\phi}_0, \hat{\phi}_1, \cdots, \hat{\phi}_M\right]^{\mathrm{T}}$ be the outputs of our DNN which is also the last layer of the MLP. In addition, to guarantee the constraints of $\hat{\phi}_i$, a sigmoid layer is utilized at the output

layer of the MLP. In other words, the normalized phase is the output of the MLP, which can be written as

$$\hat{\boldsymbol{\phi}} = \mathbf{c}_L = \mathrm{Sig}\left(\mathbf{W}_L \mathbf{c}_{L-1} + \mathbf{b}_L\right), \tag{34}$$

where $\mathrm{Sig}(.)$ denotes the standard sigmoid function.

C. Training Strategy

The performance of a DNN largely depends on how it is trained. The training process should normally be performed offline at the control center since it might consume excessive resources. In the case when a supervised learning method is utilized, the labels $\{\phi_i\}$ need to be obtained, which is time and labor consuming. By contrast, the unsupervised DL technique does not require any labels.

1) Loss function: Our proposed DNN is trained so that the upper bound of the total ergodic SE is maximized without any labels. In particular, the following loss can be set for our DNN

$$\mathcal{L}\left(\boldsymbol{\phi}, \mathcal{P}\right) \triangleq - \sum_{\{\mathbf{F},\mathbf{R},\mathbf{A}\}\in\mathcal{P}} \log_2(1 + \mathbf{F} + \mathbf{R}\left\|\mathbf{A}\boldsymbol{\phi}\right\|^2). \tag{35}$$

During the training, the weights and biases of the DNN are optimized such as the loss is minimized, or equivalently, the upper bound of the total ergodic SE is maximized.

2) Data normalization: Data normalization plays an important role in training a DNN. In [27], a point-to-point communication was considered where the path-loss shows an insignificant impact on the training process since the optimal phase shifts totally depend on the small-scale fading coefficients. In this case, the input data (i.e., small-scale fading coefficients) follows a normal distribution, which is favourable for training and does not require data normalization. In comparison, in this work, multiple CHs contribute differently to the total ergodic SE depending on their locations. Moreover, each component in the term $\mathbf{F}$ and $\mathbf{R}$ contains f_k and r_k, which are extremely low. This might lead to vanishing gradient problem in which the computed gradient values are very low, effectively preventing the weights from changing its value. To cope with this, we normalize $\mathbf{F}$ and $\mathbf{R}$ as

$$\mathbf{F}_{\mathrm{normalize}} \triangleq \frac{10\log_{10}(\mathbf{F}) - \mathrm{mean}\left(10\log_{10}(\mathbf{F})\right)}{\mathrm{var}\left(10\log_{10}(\mathbf{F})\right)^{1/2}}, \tag{36}$$

$$\mathbf{R}_{\mathrm{normalize}} \triangleq \frac{10\log_{10}(\mathbf{R}) - \mathrm{mean}\left(10\log_{10}(\mathbf{R})\right)}{\mathrm{var}\left(10\log_{10}(\mathbf{R})\right)^{1/2}}. \tag{37}$$

It is also very important to note that the true value of $\mathbf{F}$ and $\mathbf{R}$ need to be recovered from $\mathbf{F}_{\mathrm{normalize}}$ and $\mathbf{R}_{\mathrm{normalize}}$ in the implementation of the loss function. Nevertheless, there is no need to normalize $\mathbf{A}$ since its real and imaginary values range between 0 and 1.

3) Dataset generation: Since the statistical CSI is known, the dataset can be generated numerically. In particular, the positions of all CHs are generated randomly within the considered area while the transmit power of BS is generated using an uniform distribution in a range of $[\mathrm{P}_{\min}, \mathrm{P}_{\max}]$ with $\mathrm{P}_{\min}$ and $\mathrm{P}_{\max}$ standing for the minimum and maximum transmit power of BS. This process is repeated until a desirable number of data samples (i.e., $\{\mathbf{F}, \mathbf{R}, \mathbf{A}\}$) is collected, which constructs a dataset. Subsequently, this data can be partitioned into 2 datasets: training and validation set.

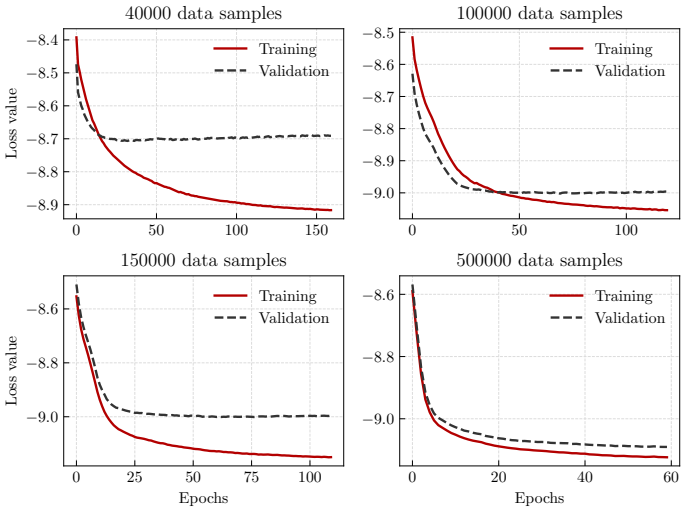

Fig. 2. The loss values over epochs for training and validation process in the case when $40000, 100000, 150000$ and 500000 data samples are used. In this simulation, $K = 3, M = 100$.

4) Impact of dataset size: To investigate the impact of dataset size on the quality of training process, we plot Fig. 2 which shows the loss computed on the training and validation set over the evolution of epochs. In this simulation, $K = 3, M = 100$ and the datasets consisting of $40000, 100000, 150000$ and 500000 data samples. In addition, 80% of the dataset was used for training and the remaining was for the validation process. As can be seen, in the case when $40000, 100000$ and 150000 data samples were used, despite the fact that the learning curves for the training and validation process show an improvement over the first 20 epochs, a remarkably large gap still remains between the both. This points out that the under-representative phenomenon occured in these cases, which means that these training datasets do not provide sufficient information to solve the problem well, relative to the validation data set used to evaluate it. By contrast, in the case when a sufficient amount of data was used (e.g., 500000 samples), the both learning curves show a satisfactory pattern in improvement. This experiment points out that a sufficiently large amount of data is neccessary for achieving a decent DNN model. Nevertheless, an issue associated with this is that the dataset might occupy huge memory resource. For instance, with 500000 data samples generated, in the case when $K = 3, M = 100$, each tensor $\mathbf{A}$ contains 300 complex numbers, which occupies approximately a memory of nearly 3.6 Gigabytes. The size of occupied memory even increases in proportion to the number of clusters and RIS size. A huge dataset consumes huge memory resources, which might cause the phenomenon of RAM overloaded in training session. To overcome this issue, we propose that only necessary information to construct $\mathbf{A}$ is stored. To this end, we rewrite $\widetilde{\mathbf{a}}_k$ as

$$\begin{aligned}\widetilde{\mathbf{a}}_k &= \mathbf{a}_k^{\mathrm{H}} \odot \mathbf{a}_0 = \mathbf{a}(\sin(\omega_k), M)^{\mathrm{H}} \odot \mathbf{a}(\sin(\omega_0), M) \\ &= \mathbf{a}(\sin(\omega_0) - \sin(\omega_k), M).\end{aligned} \tag{38}$$

This formula indicates that $\widetilde{\mathbf{a}}_k$ can totally be constructed from $\triangle\omega_k \triangleq \sin(\omega_0) - \sin(\omega_k)$. Therefore, instead of storing the

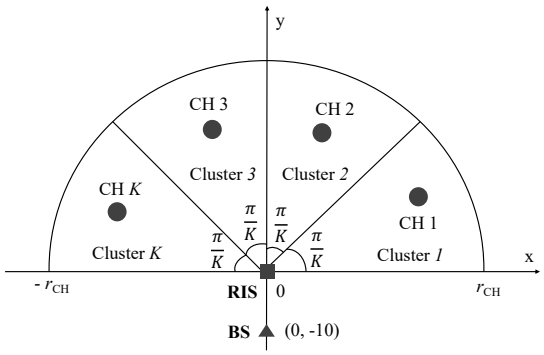

Fig. 3. The layout of IIoT network used for the simulation.

entire data of $\mathbf{A}$, we only need to store the information of $\boldsymbol{\omega} \triangleq [\triangle\omega_1, \triangle\omega_2, \cdots, \triangle\omega_K]^{\mathrm{T}}$. Apparently, the size of this new data can be reduced by M times compared to the size of $\mathbf{A}$. This is very effective especially in the case when M is large, e.g., $M > 1000$, as it reduces the data size from Gigabytes to Megabytes. We also note that the architecture of the proposed DNN still remains the same. During training process, each batch of $\boldsymbol{\omega}$ will be computed to reconstruct each batch of $\mathbf{A}$ via (38), which will subsequently be fed into the proposed DNN.

D. Online Phase Control

Once the proposed DNN is trained and fine-tuned off-line in data center, it will be stored in Controller for online inference. In each time slot, the protocol for broadcast downlink transmission can be summarized as follows

- *Step 1:* After estimating the CSI distribution, BS constructs the inputs $\mathbf{F}, \mathbf{R}$ and $\mathbf{A}$.
- *Step 2:* BS normalizes $\mathbf{F}, \mathbf{R}$ and $\mathbf{A}$ using (36).
- *Step 3:* BS sends the normalized data to Controller via wired connection.
- *Step 4:* Controller determines normalized phase shifts using the trained DNN. Subsequently, these values will be multipled with 2π to obtain the final phase shifts.
- *Step 5*: BS broadcasts signals while RIS is operating with the final phase shifts determined from *Step 4*.

It is worth noting that in the case when RCG scheme is utilized, *Step 2* is not needed and Algorithm 1 should be utilized in *Step 4*.

VI. Numerical Results and Discussions

A. Large-Scale Fading Model and Rician $\mathcal{K}$ Factor

The large-scale fading coefficient β_k contains the path-loss and shadow fading, according to

$$\beta_k = \mathrm{PL}_k \cdot 10^{\frac{\sigma_{\mathrm{sh}} z_k}{10}}, \tag{39}$$

where PL_k represents the path-loss while $10^{\frac{\sigma_{\mathrm{sh}} z_k}{10}}$ stands for the shadow fading with the standard deviation σ_{sh}, and $z_k \sim \mathcal{N}(0,1)$.

TABLE I
SYSTEM PARAMETERS USED FOR THE SIMULATIONS

Parameters	Value
Operating frequency	2.45 GHz
Bandwidth	10.0 MHz
Minimum transmit power ($\mathrm{P}_{\min}$)	$+0$ dBm
Maximum transmit power ($\mathrm{P}_{\max}$)	$+40$ dBm
Noise figure	9 dB
Shadowing standard deviation (σ)	8.13 dB
SE threshold (R_{th})	1.0 bits/s/Hz

1) Path Loss Model: We use an industrial indoor model proposed in [28] to simulate the path loss in the IIoT environment. Particularly, the path-loss (measured in dB) is calculated as $PL(D_k) = 71.84 + 21.6\log_{10}(D_k/15)$, where D_k is the length of the considered link (measured in meters). In addition, the shadowing standard deviation is set to 8.13 dB, according to [28].

2) Rician $\mathcal{K}$ Factor: It is worth noting that the Rician $\mathcal{K}$-factor and large-scale fading coefficients vary depending on the locations of CHs. In order to reflect the realistic environment in IIoTs where a direct communication link might be blocked, we use the following formulation as in [29]:

$$\mathcal{K}_k = \frac{P_{\mathrm{LOS}}(D_k)}{1 - P_{\mathrm{LOS}}(D_k)}, \tag{40}$$

where P_{LOS} is defined as in [30]:

$$P_{\mathrm{LOS}}(D_k) = \begin{cases} 1, & \text{if } D_k \leq 1\mathrm{m} \\ \exp\left(-\frac{D_k - 1}{4.9}\right), & \text{if } 1\mathrm{m} < D_k < 9.8\mathrm{m} \\ 0.17, & \text{if } D_k \geq 9.8\mathrm{m} \end{cases} \tag{41}$$

where D_k is measured in meters.

B. Parameters and Setup

For all of the considered examples, we choose the parameters summarized in Table I. In the simulation, all the clusters are located evenly within a semicircular area (so-called CH region) whose the center is at $(0, 0)$ and the radius is r_{CH}. Each cluster takes place of an arc within the semicircle with a size depending on the number of clusters in the network.[2] Furthermore, the area of cluster k is an arc with a length between $\frac{\pi(k-1)}{K}$ and $\frac{\pi k}{K}$ as illustrated in Fig. 3. To take the random effect of CH assignment mechanism within each cluster into account, for each realization generated by the simulation, all of the cluster area are kept unchanged while each CH is distributed randomly in its cluster region. In our simulations, the locations (measured in meters) of RIS and BS are fixed at $(0, 0)$ and $(0, -10)$, respectively and we select $r_{\mathrm{CH}} = 50$ m. There were 1000 realizations of the

[2]This is to guarantee that all the clusters are distributed evenly in the region since in the layout of smart factories, each production line might form a sensor cluster and all the clusters locate evenly within the smart factory area. This is for the purpose of evaluation only and does not affect the key insight. In general, the DNN methods can be used for any layouts. To do this, for a specific layout, a dataset needs to be collected first. Subsequently, the DNNs will be trained using this dataset. Over the training, the DNNs will learn the mapping between the channel coefficients and the RIS configurations so that the total ergodic spectral efficiency is maximized.

locations of CHs and shadowing profiles generated during the evaluation. The AoA for all the RIS-related signals were generated randomly. In addition, the noise power is given by

$$\sigma^2 = \text{bandwidth} \times k_B \times T_0 \times \text{noise figure}, \quad (42)$$

where $k_B = 1.381 \times 10^{-23}$ (Joule per Kelvin) is the Boltzmann constant and $T_0 = 290$ (Kelvin) is the noise temprature.

As a benchmark, we consider the following schemes:

- *RCG scheme:* The phase shifts are obtained by using RCG method described in Section IV. The settings for parameters utilized in this scheme are: $\beta = 0.5, c_1 = 0.5, N_{\text{iter}} = 100000$ and $\varepsilon = 10^{-5}$.
- *DNN scheme:* The phase shifts are obtained by using DNN method described in Section V.
- *Random scheme:* The phase shifts are generated randomly in a range of $[0, 2\pi]$.

In the special case when $K = 1$, we also investigate the following methods:

- *Optimal scheme with statistical CSI:* The optimal phase shifts are obtained by using Proposition 1 in the case when only distribution of CSI is available.
- *Optimal scheme with perfect CSI:* The optimal phase shifts are obtained in the case when the perfect CSI is available in every timeslots. The optimal phase shifts can be solved as $\boldsymbol{\phi}_{\text{optCSI},K=1} \triangleq \angle\left(\mathbf{h}_k^{\text{H}} \odot \mathbf{h}_0\right)$. The proof is omitted due to its simplicity.

When it comes to the DNN scheme, we use 2 hidden layers for the MLP with 250 neurons for each (i.e., $L = 3$, $l_1 = l_2 = 250$). The batch size is set to 40 while the learning rate is 10^{-3}. There were 400000 and 100000 data samples used for training DNN and the validation process, respectively. In this paper, all DNNs were trained using a computer with system specifications including an Intel Core i7-9700 CPU and 16 Gb of RAM. Note that the training time varies depending on the number of clusters and RIS size. Nonetheless, all the trained DNNs took just less than three hours to reach a convergence. Despite a relatively long time spent on training, the trained DNNs are fast at the online inference. This will be discussed in more detail later in this section.

C. Results and Discussions

1) Total ergodic SE evaluation: Fig. 4 compares the average ergodic SE achieved under the DNN technique with the optimal and random schemes in the case when $K = 1$. Note that the RCG algorithm achieves an identical performance compared to the optimal scheme when only the distribution of CSI is avaiable owing to the customized phase initialization. As can be seen, compared to the optimal scheme when only the distribution of CSI is known, the DNN technique shows a slight reduction in the average ergodic SE, which are nearly 0.06 and 0.14 bits/s/Hz for the case when $M = 100$ and $M = 200$, respectively (considering P = 30 dBm). Nevertheless, these figures are extremely low (less than 3% of the average optimal ergodic SE), which proves that the DNN scheme is efficient. When it comes to the random method, using up to 200 random phase shifts still acquires a remarkably lower performance compared to using just 100

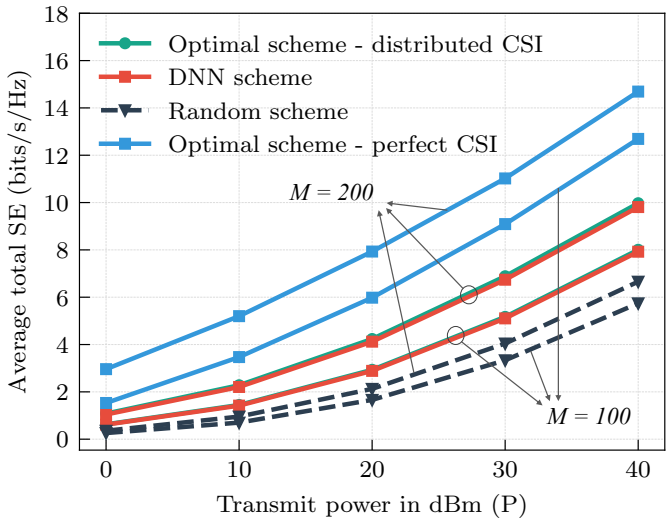

Fig. 4. Average total ergodic SE versus transmit power under the DNN, optimal and random schemes. In this simulation, $K = 1$ and $M = 100, 200$.

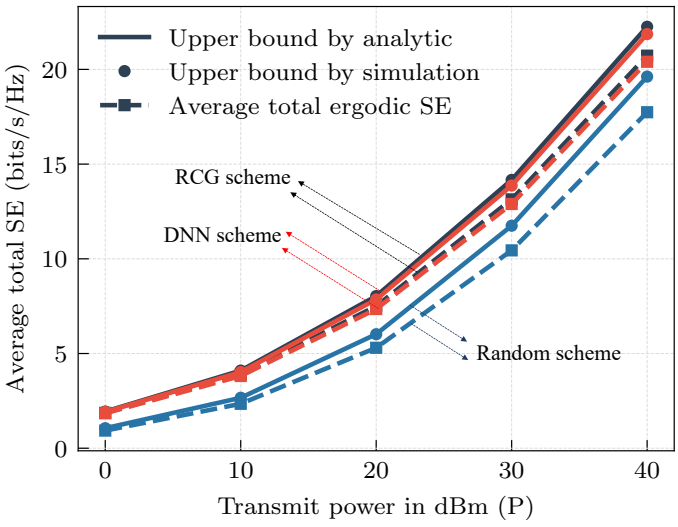

Fig. 5. Total ergodic SE versus transmit power under the DNN, RCG and random schemes. In this simulation, $K = 3$ and $M = 100$. The DNN, RCG and random schemes are represented by the black, red and dark blue color, respectively.

phase shifts determined by the DNN. This indicates that phase shift control is playing an important role in RIS-assisted wireless communications. Interestingly, utilizing the distributed CSI can still achieve around 70% the performance obtained in the case when the perfect CSI is available. This result shows that obtaining CSI might increase the total SE even further, however, at the expense of extra computational time and complexity [31].

Figure 5 demonstrates the average total ergodic SE acquired under the DNN, RCG and random schemes for the case when $K = 3$ and $M = 100$. As can be seen, both of the RCG and DNN scheme outperform the random algorithm. For instance, considering P = 30 dBm, utilizing DNN results in a significant improvement of approximately 2.45 bits/s/Hz compared to using random phases (which is equivalent to an

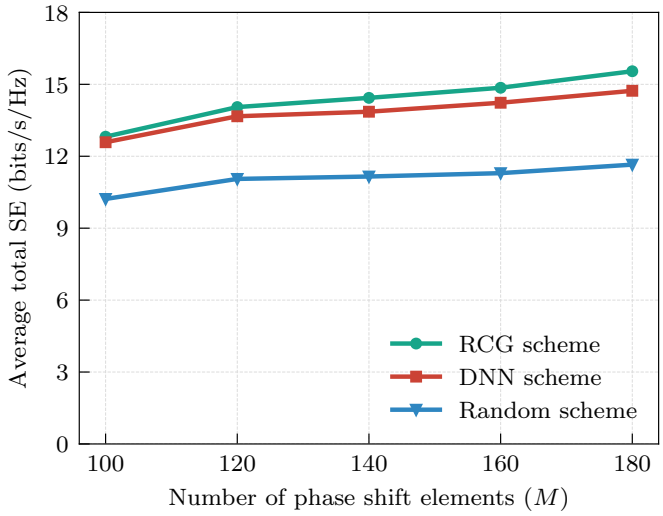

Fig. 6. Average total ergodic SE versus number of phase shift elements (M) at RIS under the DNN, RCG and random schemes. In this simulation, $K = 3$ and $\mathrm{P} = 30$ dBm.

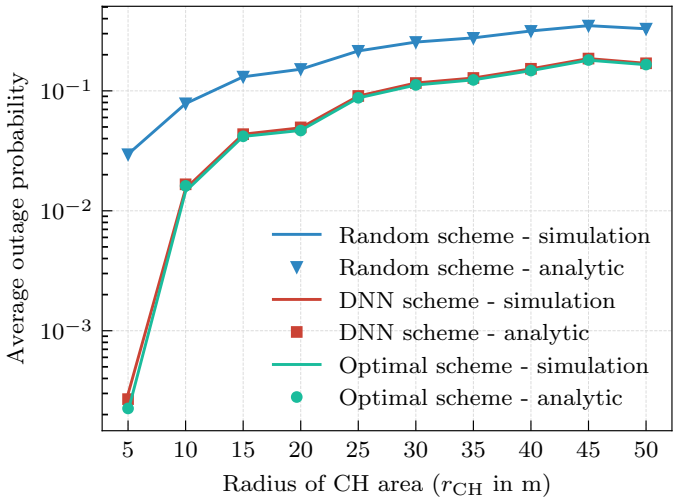

Fig. 7. Average outage probability versus the radius of CH area (r_{CH}) under the DNN, optimal and random schemes for the case when $K = 1$, $M = 100$ $\mathrm{P} = 30$ dBm.

improvement of 23%). In addition, the performance acquired by the RCG and DNN algorithms are nearly identical. Fig. 5 also demonstrates the tightness between the total ergodic SE and its upper bound. It is important to note that the difference between them tends to enlarge when the transmit power at BS increases. However, solving the sub-optimization problem still enhances the network performance remarkably. Thus, we omit the upper bound analysis in the next results.

We investigate how the number of phase shift elements impact the averate total ergodic SE of the DNN, RCG and random method, which is represented in Fig. 6. In this simulation, $K = 3$ and $\mathrm{P} = 30$ dBm. Similar to the insight obtained from Fig. 5, both of the DNN and RCG scheme provide a remarkably greater performance compared to the random method. In addition, the observation is that increasing the number of phase shift elements at RIS leads to a noticeable improvement of the average total ergodic SE. In particular, considering RCG and DNN scheme, utilizing 180 phase shift elements result in an improvement of approximately 3 bits/s/Hz compared to the case when only 100 phase shift elements are used. In comparison, regarding the random method, the amount of performance improvement is just less than 2 bits/s/Hz, which again emphasizes the importance of phase shift control. Furthermore, in all the considered values of M, the average ergodic SE achieved by DNN scheme is still slightly lower than that acquired by RCG method. This is mainly because while the RCG algorithm is guaranteed to find a local optimal solution for the optimization problem (P2), the DNN method only learns to generalize the pattern between the input coefficients and optimal phase shifts. However, the striking point is that the differences between these two algorithms are insignificant, which are merely $1.8\%, 2.8\%, 4.1\%, 4.3\%$ and 5.5% for the case when M is $100, 120, 140, 160$ and 180, respectively. As can be seen, the performance gap tends to increase when the number of phase shift elements increases. This is because an identical number of data samples (i.e., 400000) was used for training all the DNNs in this simulation. In other words, while using 400000 data samples is sufficient for training a decent DNN for the case when $M = 100$, more data might be required to achieve a better DNN in the case when $M > 100$.

2) Outage probability evaluation: Figure 7 depicts the average outage probability achieved by the DNN, optimal and random scheme with various radius values of CH region (r_{CH}) for the case when $K = 1$ and $M = 100$. Note that in this case, the RCG algorithm achieves the optimal performance. As can be clearly seen, increasing r_{CH} leads to an increase of outage probability since when r_{CH} increases, it is more likely that CHs are further away from RIS. In addition, the DNN and optimal scheme, which achieve nearly identical outage probability in all cases, outperform the random method significantly. For instance, to guarantee an outage probability of 0.1, the random scheme is only suitable for a CH region whose the radius is less than 12 m while the DNN and RCG is capable of supporting the broadcast transmissions in an area with nearly double size (25 m). It is also worth noting that when r_{CH} is large (e.g., 50 m), the outage probability is very high despite of a relatively high ergodic SE achieved. This is because the instanteous CSI is unknown, which causes a high variance in the average total SE achieved. Fig. 7 also validates the tightness of the proposed approximation for outage probability which is very close to the simulated values.

Figure 8 demonstrates the impact of r_{CH} on the average outage probability in the case when $K = 3$ and $M = 180$. Similar to the insight obtained from Fig. 7, the DNN and RCG scheme outperforms random method noticeably while showing a nearly similar outage probability. In particular, to achieve an outage probability of 0.1, utilizing random phase shifts is capable of supporting a CH area of 40m while the DNN and RCG method can be utilized to acquire the same performance for a greater area (e.g., more than 50m). This result also points out that by optimizing the total SE, the outage probability can

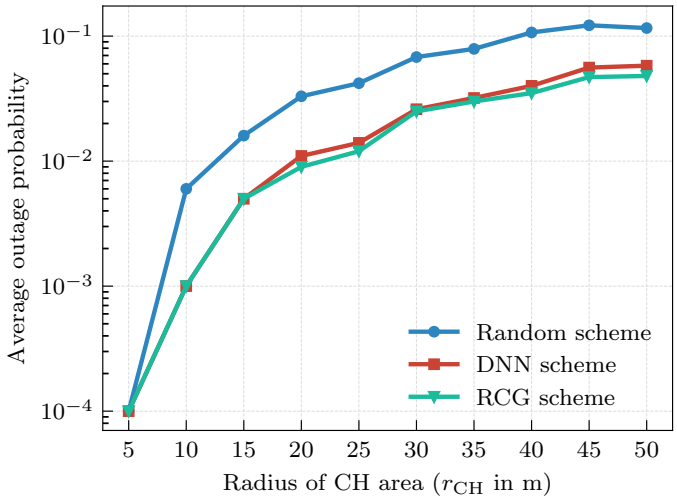

Fig. 8. Average outage probability versus the radius of CH area (r_{CH}) under the DNN, RCG and random schemes for the case when $K = 3$, $M = 180$ and $\mathrm{P} = 30$ dBm.

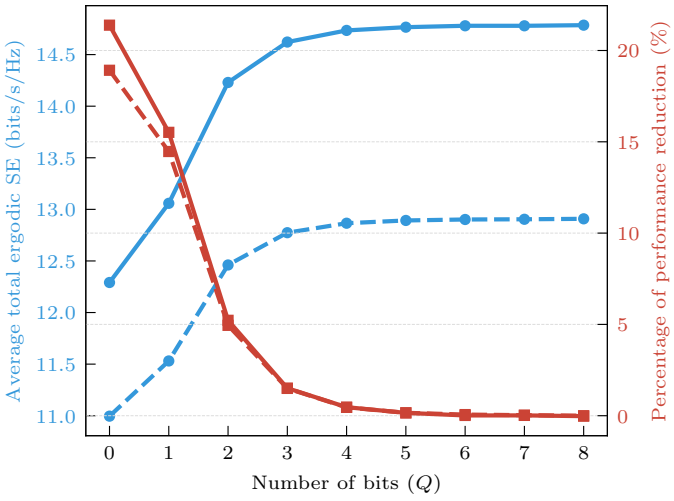

Fig. 9. The impact of number of bits (Q) on the average total ergodic SE and performance reduction for the case when $K = 3$ and $\mathrm{P} = 30$ dBm. The continuous and dashed lines represent the case when $M = 180$ and $M = 100$, respectively.

TABLE II
COMPARISON OF RUNNING TIME (SECONDS) OF DNN AND RCG SCHEME OVER 1000 REALIZATIONS.

M	DNN	RCG scheme with customized initialization	RCG scheme with random initialization
100	0.050	0.591	1.296
120	0.053	0.714	1.401
140	0.052	0.824	1.534
160	0.055	0.984	2.191
180	0.052	1.149	3.319

also be enhanced significantly.

3) Computational complexity evaluation: Table II shows the average computing time (in seconds) that the DNN and RCG scheme require to compute the phase shifts for various number of phase shift elements. Here, we consider 2 cases for RCG scheme: (1) with random initialization and (2) with proposed initialization. Interestingly, the average run time that DNN spent on the inference remains almost unchanged for every considered values of M, which are nearly 0.05 seconds. This is because except for the output layer whose size is equal to M, the remaining structure of the deep neural networks are identical for the all values of M. In comparison, with proposed initialization, the RCG scheme still requires a significantly longer computing time (e.g., more than 10 times) to generate phase shifts for each realization due to the iterative process. Nevertheless, with random initialization, the RCG scheme results in a longest computing time (e.g., double time is required in the case when $M = 100$ compared to customized initialization method). This is because with the customized initialization, the initialized phase is more closed to the local optimal solution than random one in the majority of cases. It is also worth noting that the larger RIS results in a prolonged latency for the RCG scheme to generate the phase shifts. This result reveals that utilizing the conventional iterative algorithm (such as RCG scheme) may not be suitable for phase shift control in the context of URLLC in IIoTs. By contrast, machine learning shows much potential owing to the superior computational speed and satisfactory SE performance.

4) The impact of quantized phase shifts: In practice, the phase shift values are quantized in a number of bits Q instead of being represented in a continuous space. For example, the ideal feasible set $[0, 2\pi]$ is quantized into 2^Q uniformly spaced discrete points as

$$\phi_i \in \mathcal{Q} \triangleq \left\{ \frac{2\pi}{2^Q} m \right\}_{m=0}^{2^Q-1}, i = 1, 2, \cdots, M. \quad (43)$$

To come up with such quantization, the continuous phases achieved by using DNN or RCG schemes are simply projected onto the closest point in $\mathcal{Q}$. This quantization process might cause performance reduction depending on the number of bits Q. To investigate this phenomenom, we plot Fig. 9 to represent the impact of the number of bits (Q) on the achieved total ergodic SE and percentage of performance reduction for the case when $K = 3$ and $M = 100, 180$. Here, we define the percentage of performance reduction as

$$\left(\frac{\text{Total SE ergodic by continuous phase}}{\text{Total SE ergodic by quantized phase}} - 1 \right) \times 100\%. \quad (44)$$

It can be clearly seen that for the both values of M, utilizing more number of bits to represent the phase shift provides an improved total ergodic SE. It is striking that in the case when Q is low (e.g., $Q \leq 2$), there is a remarkable difference between the average ergodic SE's achieved when Q changes. By contrast, the amount of performance improvement is insignificant when Q is sufficiently large (i.e., $Q \geq 3$). This points out that using around 3 bits is sufficient for representing the phase values.

VII. Conclusions

We investigate the use of RIS to assist the broadcast communications in IIoTs. Since blockages are encountered frequently in the smart factory environment, we consider a system model

in which RIS is used to reflect the broadcast signal from BS toward sensor clusters. In this research, instead of assuming that the perfect CSI is available, only the statistical CSI is required for signal processing. In order to control the phase shift elements effectively, two schemes are introduced, namely RCG and DNN scheme. In particular, while RCG algorithm is based on the conventional Riemmanian conjugate gradient method, DNN scheme deploys unsupervised DL technique. The results show that the both proposed techniques are effective in terms of the total ergodic SE. However, the DNN method needs only $1/10$ the time required by the RCG scheme for signal processing. This emphasizes the potential of machine leaning for URLLC applications in IIoTs.

VIII. APPENDIX

A. Proof of Lemma 1

We start to prove *Lemma* 1 by computing the expression of $\mathbb{E}\{\left\|\mathbf{h}_k^{\mathrm{H}}\mathbf{\Phi}\mathbf{h}_0\right\|^2\}$. Denote $\mathbf{A} \triangleq \mathbb{E}\left\{\mathbf{\Phi}^{\mathrm{H}}\mathbf{h}_k\mathbf{h}_k^{\mathrm{H}}\mathbf{\Phi}\right\}$, according to [32, 6.2.2], $\mathbf{A}$ is calculated as

$$\begin{aligned}\mathbf{A} &= \mathbf{\Phi}^{\mathrm{H}}\left(\mathrm{cov}(\mathbf{h}_k) + \mathrm{mean}(\mathbf{h}_k)^{\mathrm{H}}\mathrm{mean}(\mathbf{h}_k)\right)\mathbf{\Phi} \\ &= \mathbf{\Phi}^{\mathrm{H}}\left(\frac{\beta_k}{\mathcal{K}_k+1}\mathbf{I}_M + \bar{\mathbf{h}}_k\bar{\mathbf{h}}_k^{\mathrm{H}}\right)\mathbf{\Phi} \\ &= \frac{\beta_k}{\mathcal{K}_k+1}\mathbf{I}_M + \mathbf{\Phi}^{\mathrm{H}}\bar{\mathbf{h}}_k\bar{\mathbf{h}}_k^{\mathrm{H}}\mathbf{\Phi}.\end{aligned} \tag{45}$$

Since $\mathbf{h}_0$ and $\mathbf{h}_k$ are independent, $\mathbb{E}\{\left\|\mathbf{h}_k^{\mathrm{H}}\mathbf{\Phi}\mathbf{h}_0\right\|^2\}$ can be rewritten as

$$\begin{aligned}&\mathbb{E}\{\left\|\mathbf{h}_k^{\mathrm{H}}\mathbf{\Phi}\mathbf{h}_0\right\|^2\} = \mathbb{E}\left\{\mathbf{h}_0^{\mathrm{H}}\mathbf{A}\mathbf{h}_0\right\} \\ &\overset{(a)}{=} \mathrm{Tr}(\mathbf{A}\ \mathrm{cov}(\mathbf{h}_0)) + \mathrm{mean}(\mathbf{h}_0)^{\mathrm{H}}\mathbf{A}\ \mathrm{mean}(\mathbf{h}_0) \\ &= \frac{\beta_0}{\mathcal{K}_0+1}\mathrm{Tr}(\mathbf{A}) + \bar{\mathbf{h}}_0^{\mathrm{H}}\mathbf{A}\bar{\mathbf{h}}_0 \\ &= \frac{\beta_0}{\mathcal{K}_0+1}\left(\frac{M\beta_k}{\mathcal{K}_k+1} + \mathrm{Tr}(\mathbf{\Phi}^{\mathrm{H}}\bar{\mathbf{h}}_k\bar{\mathbf{h}}_k^{\mathrm{H}}\mathbf{\Phi})\right) + \frac{\beta_k}{\mathcal{K}_k+1}\bar{\mathbf{h}}_0^{\mathrm{H}}\bar{\mathbf{h}}_0 \\ &+ \bar{\mathbf{h}}_0^{\mathrm{H}}\mathbf{\Phi}^{\mathrm{H}}\bar{\mathbf{h}}_k\bar{\mathbf{h}}_k^{\mathrm{H}}\mathbf{\Phi}\bar{\mathbf{h}}_0 \\ &\overset{(b)}{=} \frac{M\beta_0\beta_k}{(\mathcal{K}_0+1)(\mathcal{K}_k+1)} + \frac{\beta_0}{\mathcal{K}_0+1}\bar{\mathbf{h}}_k^{\mathrm{H}}\bar{\mathbf{h}}_k + \frac{\beta_k}{\mathcal{K}_k+1}\bar{\mathbf{h}}_0^{\mathrm{H}}\bar{\mathbf{h}}_0 \\ &+ \left\|\bar{\mathbf{h}}_k^{\mathrm{H}}\mathbf{\Phi}\bar{\mathbf{h}}_0\right\|^2,\end{aligned} \tag{46}$$

where the transformation (a) was utilized by using [32, 7.2.2] while the transformation (b) was due to the fact that $\mathbf{\Phi}$ is a diagonal matrix, which means $\mathrm{Tr}(\mathbf{\Phi}^{\mathrm{H}}\bar{\mathbf{h}}_k\bar{\mathbf{h}}_k^{\mathrm{H}}\mathbf{\Phi}) = \bar{\mathbf{h}}_k^{\mathrm{H}}\bar{\mathbf{h}}_k$. From (46), by noting that $\mathbf{a}_k^{\mathrm{H}}\mathbf{a}_k = \mathbf{a}_0^{\mathrm{H}}\mathbf{a}_0 = M$, $\bar{\mathbf{a}}_k^{\mathrm{H}}\mathbf{\Phi}\bar{\mathbf{a}}_0 = \widetilde{\mathbf{a}}_k^{\mathrm{H}}\boldsymbol{\phi}$ and adopting the definition of $\mathbf{h}_0$ and $\mathbf{h}_k$, the proof is completed.

B. Proof of Lemma 2

By applying the Jensen's inequality, we have

$$\begin{aligned}\mathbb{E}\left\{\log_2(1+\gamma_k)\right\} &\le \log_2(1+\mathbb{E}\left\{\gamma_k\right\}) \\ &= \log_2\left(1+\frac{\mathrm{P}}{\sigma^2}\mathbb{E}\{\left\|\mathbf{h}_k^{\mathrm{H}}\mathbf{\Phi}\mathbf{h}_0\right\|^2\}\right).\end{aligned} \tag{47}$$

By using the *Lemma* 1 and (11), the proof is directly obtained.

C. Proof of Lemma 3

In the case when the number of phase elements at RIS is sufficiently large, according to the central limit theorem [33], the term X_k can be approximated as a complex Gaussian Y whose the first and second moments are identical to that of X_k. In other words, we let $\mathrm{X}_k \approx \mathrm{Y}$, where $\mathrm{Y} \sim \mathcal{CN}\left(\mathbf{m}_{\mathrm{y}}, \sigma_{\mathrm{y}}^2\right)$ with $\mathbf{m}_{\mathrm{y}}$ and σ_{y}^2 standing for the mean vector and variance of Y. In addition, $\mathbb{E}\{\mathrm{Y}\} = \mathbb{E}\{\mathrm{X}_k\}$ and $\mathbb{V}\{\mathrm{Y}\} = \mathbb{V}\{\mathrm{X}_k\}$. As a result, $\mathbf{m}_{\mathrm{y}}$ and σ_{y}^2 can be determined as

$$\begin{aligned}\mathbf{m}_{\mathrm{y}} &= \bar{\mathbf{h}}_k^{\mathrm{H}}\mathbf{\Phi}\bar{\mathbf{h}}_0, \\ \sigma_{\mathrm{y}}^2 &= \mathbb{E}\{\mathrm{X}_k^2\} - \mathbb{E}\{\mathrm{X}_k\}^2.\end{aligned} \tag{48}$$

By using *Lemma* 1 along with several basic mathematical transformations, we obtain

$$\mathbf{m}_{\mathrm{y}} = \left(r_k\frac{\sigma^2}{\mathrm{P}}\right)^{1/2}\left\|\widetilde{\mathbf{a}}_k^{\mathrm{H}}\boldsymbol{\phi}\right\|, \tag{49}$$

$$\sigma_{\mathrm{y}}^2 = M\beta_0\beta_k\frac{\mathcal{K}_0\mathcal{K}_k+1}{(\mathcal{K}_0+1)(\mathcal{K}_k+1)} = \frac{\sigma^2}{\mathrm{P}}f_k. \tag{50}$$

To compute (13), we rewrite Y as $\mathrm{Y} = \mathrm{Y}_{\mathrm{re}} + j\mathrm{Y}_{\mathrm{im}}$ with $\mathrm{Y}_{\mathrm{re}} = \Re(\mathrm{Y})$ and $\mathrm{Y}_{\mathrm{im}} = \Im(\mathrm{Y})$. As a consequence, $\mathrm{Y}_{\mathrm{re}} \sim \mathcal{CN}(\Re(\mathbf{m}_{\mathrm{y}}), \frac{\sigma_{\mathrm{y}}^2}{2})$ and $\mathrm{Y}_{\mathrm{im}} \sim \mathcal{CN}(\Im(\mathbf{m}_{\mathrm{y}}), \frac{\sigma_{\mathrm{y}}^2}{2})$. Now, let $\bar{\mathrm{Y}} \triangleq \frac{\sqrt{2}}{\sigma_{\mathrm{y}}}\mathrm{Y}$ and $\bar{\mathrm{Y}} = \bar{\mathrm{Y}}_{\mathrm{re}} + j\bar{\mathrm{Y}}_{\mathrm{im}}$. It is obvious that $\bar{\mathrm{Y}}_{\mathrm{re}} \sim \mathcal{CN}(\frac{\sqrt{2}}{\sigma_{\mathrm{y}}}\Re(\mathbf{m}_{\mathrm{y}}), 1)$ and $\bar{\mathrm{Y}}_{\mathrm{im}} \sim \mathcal{CN}(\frac{\sqrt{2}}{\sigma_{\mathrm{y}}}\Im(\mathbf{m}_{\mathrm{y}}), 1)$. From here, (13) can be approximated to

$$\mathrm{P}_{\mathrm{out},k} \approx \Pr\left\{\bar{\mathrm{Y}}_{\mathrm{re}}^2 + \bar{\mathrm{Y}}_{\mathrm{im}}^2 < \frac{2}{\mathrm{P}}\frac{\sigma^2}{\sigma_y^2}(2^{R_{\mathrm{th},k}}-1)\right\}. \tag{51}$$

Since $\bar{\mathrm{Y}}_{\mathrm{re}}$ and $\bar{\mathrm{Y}}_{\mathrm{im}}$ follow Gaussian distributions with an unit variance, the term $\bar{\mathrm{Y}}_{\mathrm{re}}^2 + \bar{\mathrm{Y}}_{\mathrm{im}}^2$ follows a non-central Chi-square distribution with 2 degrees of freedom and the non-centrality parameter $\lambda \triangleq 2\frac{\mathbf{m}_{\mathrm{y}}}{\sigma_{\mathrm{y}^2}}$. By subtituting these terms into the CDF function of Chi-square distribution [34], the proof was completed.

REFERENCES

[1] M. Series, "IMT vision–framework and overall objectives of the future development of IMT for 2020 and beyond," *Recommendation ITU*, vol. 2083, 2015.

[2] Y. Liu, M. Kashef, K. B. Lee, L. Benmohamed, and R. Candell, "Wireless network design for emerging IIoT applications: reference framework and use cases," *Proc. IEEE*, vol. 107, no. 6, pp. 1166–1192, 2019.

[3] X. Pei, H. Yin, L. Tan, L. Cao, Z. Li, K. Wang, K. Zhang, and E. Björnson, "RIS-aided wireless communications: Prototyping, adaptive beamforming, and indoor/outdoor field trials," *arXiv preprint arXiv:2103.00534*, 2021.

[4] Q. Wu and R. Zhang, "Intelligent reflecting surface enhanced wireless network: Joint active and passive beamforming design," in *Proc. IEEE Globecom*, 2018, pp. 1–6.

[5] C. Huang, A. Zappone, M. Debbah, and C. Yuen, "Achievable rate maximization by passive intelligent mirrors," in *Proc. IEEE ICASSP*, 2018, pp. 3714–3718.

[6] A. Kammoun, A. Chaaban, M. Debbah, M.-S. Alouini *et al.*, "Asymptotic max-min SINR analysis of reconfigurable intelligent surface assisted MISO systems," *IEEE Trans. Wireless Commun.*, vol. 19, no. 12, pp. 7748–7764, 2020.

[7] D. Mishra and H. Johansson, "Channel estimation and low-complexity beamforming design for passive intelligent surface assisted MISO wireless energy transfer," in *Proc. IEEE ICASSP*, 2019, pp. 4659–4663.

[8] H. Alwazani, A. Kammoun, A. Chaaban, M. Debbah, M.-S. Alouini *et al.*, "Intelligent reflecting surface-assisted multi-user MISO communication: Channel estimation and beamforming design," *IEEE J. Commun. Soc.*, vol. 1, pp. 661–680, 2020.
[9] B. Deepak, R. Sankar, and S. P. Chepuri, "Channel estimation in reconfigurable intelligent surface assisted mm-Wave MIMO systems," *arXiv preprint arXiv:2011.00900*, 2020.
[10] G. Chalapathi, V. Chamola, S. Gurunarayanan, and B. Sikdar, "E-SATS: An efficient and simple time synchronization protocol for cluster-based wireless sensor networks," *IEEE Sens. J.*, vol. 19, no. 21, pp. 10 144–10 156, 2019.
[11] Z. Wang, P. Zeng, M. Zhou, D. Li, and J. Wang, "Cluster-based maximum consensus time synchronization for industrial wireless sensor networks," *Sensors*, vol. 17, no. 1, p. 141, 2017.
[12] J. Wu, L. Zhang, Y. Bai, and Y. Sun, "Cluster-based consensus time synchronization for wireless sensor networks," *IEEE Sens. J.*, vol. 15, no. 3, pp. 1404–1413, 2014.
[13] Y. Sung, S. Lee, and M. Lee, "A multi-hop clustering mechanism for scalable IoT networks," *Sensors*, vol. 18, no. 4, p. 961, 2018.
[14] W. Tang, X. Chen, M. Z. Chen, J. Y. Dai, Y. Han, S. Jin, Q. Cheng, G. Y. Li, and T. J. Cui, "On channel reciprocity in reconfigurable intelligent surface assisted wireless network," *arXiv preprint arXiv:2103.03753*, 2021.
[15] A. Kumari, S. Tanwar, S. Tyagi, and N. Kumar, "Blockchain-based massive data dissemination handling in IIoT environment," *IEEE Network*, vol. 35, no. 1, pp. 318–325, 2020.
[16] A. Sinha, G. Paschos, C.-P. Li, and E. Modiano, "Throughput-optimal multihop broadcast on directed acyclic wireless networks," *IEEE/ACM Trans. Netw.*, vol. 25, no. 1, pp. 377–391, 2016.
[17] C. W. Tan, M. Chiang, and R. Srikant, "Fast algorithms and performance bounds for sum rate maximization in wireless networks," *IEEE/ACM Trans. Netw.*, vol. 21, no. 3, pp. 706–719, 2012.
[18] H. Al-Shatri and T. Weber, "Optimizing power allocation in interference channels using DC programming," in *Proc. IEEE WiOpt*, 2010, pp. 360–366.
[19] M. Codreanu, A. Tolli, M. Juntti, and M. Latva-Aho, "Joint design of Tx-Rx beamformers in MIMO downlink channel," *IEEE Trans. Signal Process.*, vol. 55, no. 9, pp. 4639–4655, 2007.
[20] H. Sato and T. Iwai, "A new, globally convergent Riemannian conjugate gradient method," *Optimization*, vol. 64, no. 4, pp. 1011–1031, 2015.
[21] H. Oviedo and H. J. Lara, "A Riemannian conjugate gradient algorithm with implicit vector transport for optimization in the stiefel manifold," Technical report, Technical report. UFSC-Blumenau, CIMAT, Tech. Rep., 2018.
[22] H. Sakai and H. Iiduka, "Sufficient descent Riemannian conjugate gradient methods," *J. Optim. Theory Appl.*, pp. 1–21, 2021.
[23] F. Liu, C. Masouros, P. V. Amadori, and H. Sun, "An efficient manifold algorithm for constructive interference based constant envelope precoding," *IEEE Signal Process. Lett.*, vol. 24, no. 10, pp. 1542–1546, 2017.
[24] X. Yu, D. Xu, and R. Schober, "MISO wireless communication systems via intelligent reflecting surfaces," in *Proc. IEEE/CIC ICCC*, 2019, pp. 735–740.
[25] J. Nocedal and S. Wright, *Numerical optimization*. Springer Science & Business Media, 2006.
[26] T. Lin and Y. Zhu, "Beamforming design for large-scale antenna arrays using deep learning," *IEEE Signal Process. Lett.*, vol. 9, no. 1, pp. 103–107, 2019.
[27] N. T. Nguyen, L. V. Nguyen, T. Huynh-The, D. H. Nguyen, A. L. Swindlehurst, and M. Juntti, "Machine learning-based reconfigurable intelligent surface-aided MIMO systems," *arXiv preprint arXiv:2105.00347*, 2021.
[28] E. Tanghe, W. Joseph, L. Verloock, L. Martens, H. Capoen, K. Van Herwegen, and W. Vantomme, "The industrial indoor channel: large-scale and temporal fading at 900, 2400, and 5200 MHz," *IEEE Trans. Wireless Commun.*, vol. 7, no. 7, pp. 2740–2751, 2008.
[29] A. H. Jafari, D. López-Pérez, M. Ding, and J. Zhang, "Study on scheduling techniques for ultra dense small cell networks," in *Proc. IEEE. Veh. Technol. Conf.*, 2015, pp. 1–6.
[30] K. Haneda, L. Tian, H. Asplund, J. Li, Y. Wang, D. Steer, C. Li, T. Balercia, S. Lee, Y. Kim *et al.*, "Indoor 5G 3GPP-like channel models for office and shopping mall environments," in *Proc. IEEE ICC*, 2016, pp. 694–699.
[31] A. L. Swindlehurst, G. Zhou, R. Liu, C. Pan, and M. Li, "Channel estimation with reconfigurable intelligent surfaces–a general framework," *arXiv preprint arXiv:2110.00553*, 2021.
[32] K. Petersen and M. Pedersen, "The matrix cookbook. technical university of denmark," *Technical Manual*, 2008.
[33] R. D. Yates and D. J. Goodman, "Probability and stochastic processes," *John Willey & Sons*, 1999.
[34] H. O. Lancaster and E. Seneta, "Chi-square distribution," *Encyclopedia of biostatistics*, vol. 2, 2005.

Son Dinh-Van received the B.S. degree from Hanoi University of Science and Technology, Vietnam, in 2013, the M.S. degree from Soongsil University, Seoul, South Korea, in 2015, and the Ph.D. degree from Queen's University of Belfast, Belfast, U.K., in 2019, all in electrical engineering. He is currently a Research Fellow with Warwick Manufacturing Group, University of Warwick, U.K. He was a Data Scientist with Frequenz Gmbh, Germany and a Visiting Researcher with Middlesex University, U.K, in 2020 and 2021, respectively. His current research interests include massive MIMO, millimeter wave, machine learning, industrial Internet of Things and 5G/6G communications.

Tiep. M. Hoang received the B.Eng. degree from the HCMC University of Technology, Vietnam, in 2012, the M.Eng. degree from Kyung Hee University, South Korea, in 2014, and the Ph.D. degree from the Queen's University of Belfast, UK, in 2019. He is currently a Research Fellow with the School of Electronics and Computer Science, the University of Southampton, UK. His current research interests include wireless security, flying ad-hoc networks, convex optimization, and machine learning.

Ramona Trestian is a Senior Lecturer with Design Engineering and Mathematics Department, Faculty of Science and Technology, Middlesex University, London, UK. She was previously an IBM-IRCSET Exascale Postdoctoral Researcher with the Performance Engineering Laboratory (PEL) at Dublin City University (DCU), Ireland since December 2011. She was awarded the PhD from Dublin City University in March 2012 and the B.Eng. in Telecommunications from Technical University of Cluj-Napoca, Romania, 2007. She published in prestigious international conferences and journals and has five edited books. Her research interests include mobile and wireless communications, quality of experience, multimedia streaming, and digital twin modelling. She is an Associate Editor of the IEEE COMMUNICATIONS SURVEYS AND TUTORIALS .

Huan X. Nguyen (M'06–SM'15) received the B.Sc. degree from the Hanoi University of Science and Technology, Vietnam, in 2000, and the Ph.D. degree from the University of New South Wales, Australia, in 2007. He is currently a Professor of Digital Communication Engineering at Middlesex University London (U.K.), where he is also the Director of the London Digital Twin Research Centre and Head of the 5G/6G & IoT Research Group. He leads research activities in digital twin modelling, 5G/6G enabling technologies, IoT communication, and machine learning within his university with focus on digital transformation, industry 4.0 and critical applications (disasters, intelligent transportation, health). He has been leading 10+ major council/industry funded projects, publishing 120+ peer-reviewed research papers, and serving as chairs for international conferences (ICT'21, ICEM2021, ICT'20, ICT'19, IWNPD'17, PIMRC'20, FoNeS-IoT'20, ATC'15).